Tunable Optical Grating Based on the Flexoelectric Effect in a Bent-Core Nematic Liquid Crystal

Ying Xiang,[1] Hong-Zhen Jing,[1] Zhi-Dong Zhang,[3] Wen-Jiang Ye,[3] Ming-Ya Xu,[1] Everett Wang,[1] Péter Salamon,[2] Nándor Éber,[2] and Ágnes Buka[2]

[1]*School of Information Engineering, Guangdong University of Technology, Guangzhou 510006, People's Republic of China*

[2]*Institute for Solid State Physics and Optics, Wigner Research Centre for Physics, Hungarian Academy of Sciences, P.O. Box 49, H-1525 Budapest, Hungary*

[3]*School of Sciences, Hebei University of Technology, Tianjin 300401, People's Republic of China*

(Received 14 November 2016; revised manuscript received 14 March 2017; published 30 June 2017)

Optical gratings are created by flexoelectric domains in a bent-core nematic liquid crystal. A unique feature of this structure is that its wavelength can be controlled by the amplitude of the applied voltage, as demonstrated by polarizing microscopy and light diffraction techniques. In order to understand the reaction of the system to the voltage change, the dynamics of the switching process is studied via digital processing of recorded image sequences. It is shown that the characteristics and the switching mechanisms are different if the lower voltage level is below or above the threshold of pattern onset. In both cases, the response to increasing voltage levels is much slower than the response to decreasing voltage levels.

DOI: 10.1103/PhysRevApplied.7.064032

I. INTRODUCTION

The remarkable electro-optic effects of nematic liquid crystals (LCs) arise from their large optical anisotropy and their high sensitivity to external fields [1,2]. In addition to a wide range of applications in displays, LCs are now used more and more for manipulating light (including beam shaping or steering), for switchable holograms, and for other photonic applications [3–6]. This field of optical processing has become increasingly important in the information age.

Optical phase gratings play important roles in photonic devices, whose performance will determine their capability to process information. Among diverse gratings, diffraction gratings based on LCs have potential advantages over conventional holographic gratings due to the large optical anisotropies and the ability to use LCs for controllable electro-optical switching.

Usually, LC gratings are realized either by patterned electrodes [7–9] or by illumination with a spatially varying light intensity created by interference [10–13], which modulates the refractive index; in both cases, the grating morphologies are fixed. However, another kind of LC grating, which is based on self-assembled structures in LCs, can be produced by a uniform electric field applied to monolithic (nonpatterned) electrodes. Electroconvection (EC) patterns [14–16] are typical and representative cases of such gratings.

EC phenomena are distinctive features of LCs, which are fluid and ordered media; they are often manifested in the emergence of various convection rolls, which appear as a regular set of dark and bright stripes in a polarizing microscope. When driven by an electric voltage, LCs can form different kinds of EC-pattern morphologies; they arise from the couplings among the deformation of the LC orientation, the flow of both material and charge, and the applied electric field. The characteristics of the induced patterns, such as the onset voltage, the critical wave vector, and the frequency range of existence, are closely related to the dielectric and the charge-transport properties of LCs, as well as the boundary conditions [14–16]. The formation of convection rolls was explained by Carr and Helfrich [1,16] via a feedback mechanism: a periodic fluctuation in the director tilt leads to space-charge separation due to the anisotropic conductivity; the Coulomb force on the space charge induces a vortex flow, which exerts a destabilizing torque on the director. When this feedback becomes positive at voltages above a threshold U_c, the fluctuations with a selected (critical) wave vector $\mathbf{q}_c$ can grow to a macroscopic pattern.

In contrast to the current-driven EC rolls, the flexoelectric domains (FDs) [17,18] are typical field-driven patterns. They appear as a consequence of the linear coupling between the electric field $\mathbf{E}$ and the flexoelectric polarization [19,20] $\mathbf{P}_{\mathrm{fl}} = e_1\mathbf{n}\mathrm{div}\mathbf{n} - e_3\mathbf{n}\times\mathrm{curl}\mathbf{n}$ (here, e_1 and e_3 are the phenomenological flexoelectric coefficients), which yields a free energy gain in the periodically deformed state compared to the homogeneous planar initial state. FDs manifest themselves as static longitudinal (parallel to the initial director) stripes without convection, which may open up alternative possibilities for applications. The formation of these electric-field-induced gratings is, however, strongly constrained by the internal physical properties of LCs; to date, only a very few nematics have been reported to exhibit FDs [21]. As the characteristics of FDs are governed by the flexoelectric coefficients (which

have been shown to be directly linked to the molecular structure of LCs), investigation of these kinds of gratings aiming to obtain deeper insight into the pattern formation mechanism and the working principles of future devices requires one to seek alternative LC materials with special molecular structures and improved performance.

In fact, traditional LC molecules possess a rodlike shape; this molecular structure yields very small flexoelectric coefficients. Unconventional LC systems based on bent-core molecules have recently generated considerable interest since their banana-shaped molecular structure leads to peculiar physical properties [22]. Owing to the combination of the bent molecular shape and a transverse component of dipole moment, bent-core nematics (BCNs) [23] are ideal candidates for compounds with large flexoelectric coefficients. Indeed, it was reported that, under certain conditions (with flexible substrates and at a high enough electric field [24]), BCN systems may exhibit a giant flexoelectric response [25,26], corresponding to a bend flexoelectric coefficient e_3, which is several orders of magnitude greater than that of rodlike compounds. The experimental conditions for observing FDs do not conform to these requirements, so the flexocoefficients governing the electric-field-induced deformations (including FD formation) in bent-core materials are found to be similar or a little higher than those in calamitics [27,28]. Nevertheless, BCNs still offer significant potential for the observation and the application of flexoelectric domains. Therefore, in this paper, we investigate the electric-field-induced optical grating based on FDs in a bent-core nematic LC.

Most previous work on FDs has focused on their static behavior (such as the threshold voltage U_{th} and the critical wavelength Λ_{th}), which are the result of an equilibrium deformation (without any material flow). The traditional theoretical description of FDs, which is based on a linear model [17,19], can provide only U_{th} and Λ_{th}, but it does not supply information on the voltage dependence of Λ (or that of the wave number $q = |\mathbf{q}| = 2\pi/\Lambda$) for $U > U_{\mathrm{th}}$, though it would be essential for grating applications. The only available nonlinear analysis of FDs at this time [29] predicts that $q(U)$ will be proportional to the strength of the applied electric field $\mathbf{E}$. Thus, by measuring $q(U)$ in our material, we can test the applicability of this prediction. It was also found that the occurrence, as well as the polarization state, of the diffracted light strongly depends on the conditions of the light incidence.

Understanding the driving mechanisms of FDs is not complete without information on their dynamics, including how they emerge and decay, as well as how they evolve during switching. The latter is especially important concerning the applications of FDs. Therefore, in this work, we concentrate more on the dynamics of FDs. Since the wave number q is a key characteristic of FDs, we monitor the time dependence of q as a tool for analyzing the dynamic behavior of FDs systematically.

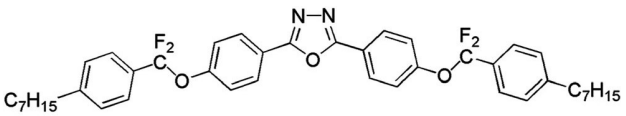

(7*P*-CF_2O-ODBP)

FIG. 1. Structural formula of the BCN compound 2,5-bis {4-[difluoro (4-heptylphenyl) methoxy] phenyl}-1,3,4-oxadiazole (7*P*-CF_2O-ODBP).

II. MATERIAL AND METHODS

Measurements are performed on the BCN compound 2,5-bis {4-[difluoro (4-heptylphenyl) methoxy] phenyl}-1,3,4-oxadiazole (7*P*-CF_2O-ODBP), whose structural formula is shown in Fig. 1. The phase sequence is crystal, 77 °C, smectic, 90.3 °C, nematic, 131.5 °C, isotropic.

The BCN samples are filled into sandwich cells of $d = 6$ μm thickness. The indium-tin-oxide electrodes are covered with a passivating layer of SiO_2 in order to prevent injection of charge carriers through the electrode, as well as with rubbed polyimide to provide planar alignment. The initial director orientation $\mathbf{n}_0$ is along the x axis, while the electric field $\mathbf{E}$ is applied along the z axis, i.e., perpendicular to the substrates and $\mathbf{n}_0$. The temperature of the samples is controlled using a Linkam LTS 350/TMS 94 hot stage.

The BCN sample is driven through a high-voltage amplifier either by constant voltage or by steplike voltage levels changing repetitively at ultralow frequency, generated by a function generator. The voltage-induced FDs are observed by a Leica DM RXP polarizing microscope (POM) in transmission mode using a single polarizer only (the shadowgraph technique [30]). In order to explore the temporal evolution of FDs, image sequences of the FD pattern are captured by a fast black-and-white camera (Mikrotron EoSens MC 1362) with an adjustable (maximum 2000 frames/s) recording rate at the spatial resolution of 520×512 pixels; the recording is synchronized with the switching of the applied voltage.

The recorded image sequences are later digitally processed for further characterization of the patterns. This procedure includes determination of the pattern contrast C, defined as the mean-square deviation of the intensities I_{xy} of the pixels of the image,

$$C = \langle (I_{xy} - \langle I_{xy} \rangle)^2 \rangle, \tag{1}$$

where $\langle \cdots \rangle$ denotes averaging over the whole image. A two-dimensional fast Fourier transform (FFT) of the images is also performed, providing the spectral distribution function $\Psi(\mathbf{q})$—the square of the absolute value of the Fourier amplitude—at the location $\mathbf{q} = (q_x, q_y)$ in the Fourier space. One can then introduce the spectral entropy [31]

$$S = -\langle P(\mathbf{q}) \ln P(\mathbf{q}) \rangle_q \tag{2}$$

as a measure of the order of the pattern, with

$$P(\mathbf{q}) = \frac{\Psi(\mathbf{q})}{\int\int \Psi(\mathbf{q}) dq_x dq_y} \tag{3}$$

being the normalized spectral distribution function; the averaging $\langle \cdots \rangle_q$ extends over the whole Fourier space. Increasing S means a reduction in the order of the pattern.

The Fourier peaks of the FD patterns are not perfectly sharp, especially after voltage transients, when the pattern contains several defects (dislocations). Therefore, instead of singling out the location $\mathbf{q}_m$ of the maximal $P(\mathbf{q})$, an averaged wave vector

$$q_{\mathrm{av}} = \int\int_A \mathbf{q} P(\mathbf{q}) dq_x dq_y \tag{4}$$

of the pattern is calculated by a weighted averaging over a closed region A surrounding the Fourier peak at $\mathbf{q}_m$.

Besides polarizing microscopy, an independent, optical diffraction technique is also used to probe the characteristics of FDs. The periodic director distortion of FDs corresponds to an optical grating, which diffracts the incident beam of a He-Ne laser ($\lambda = 633$ nm). The far-field diffraction image and the corresponding diffraction intensity of the fringes are recorded by a digital camera and a photodetector, respectively. From the position of the centers of the diffraction spots and the diffraction angles ϕ_κ of the κth order, and via the Braggs relation $\Lambda \sin \phi_\kappa = \kappa\lambda$, the pattern wavelength is determined. The ratio of the intensity I_κ of the κth-order diffraction to the intensity I_0 of the direct beam provides the diffraction efficiency of the grating.

III. EXPERIMENTAL RESULTS

In the following, we summarize the results obtained by combining the POM and diffraction techniques about the static and dynamic (switching) behavior of FD gratings at a fixed temperature of $T = 105\,^{\circ}\mathrm{C}$. In addition, we report on some unexpected polarization characteristics of the light diffracted on the FD grating that are revealed by the diffraction technique.

A. Static behavior

The dc voltage dependence of the FD pattern is demonstrated in Fig. 2 by a sequence of POM snapshots and the corresponding diffraction fringes taken at different voltages. It clearly shows that, when the applied dc voltage U exceeds a threshold U_{th} ($\lessapprox 22$ V in our case), FDs are present in the form of longitudinal stripes running parallel with $\mathbf{n}_0$ whose wavelength Λ decreases with increased voltages.

A detailed analysis of the diffracted light (determination of the diffraction angles ϕ_n of the nth order and then the wavelength Λ of the pattern from the Bragg criterion of $\Lambda \sin \phi_n = n\lambda$) proves that the wave number q of the FDs—and hence the dimensionless wave number $q^* = qd/\pi = 2d/\Lambda$ as well—depends linearly on the applied dc voltage, as shown in Fig. 3(a). Least-squares fitting provides

$$q^*(U) = q^*_{\mathrm{th}} + \alpha(U - U_{\mathrm{th}}), \tag{5}$$

where $q^*_{\mathrm{th}} = 2.53 \pm 0.18$ is the critical dimensionless wave number at the threshold U_{th} and $\alpha = 0.185 \pm 0.003\ \mathrm{V}^{-1}$ gives the slope of the $q^*(U)$ curve.

We should note at this point that the voltage applied to our cell is not equal to the voltage on the LC layer, escpecially at dc driving, due to the internal voltage attenuation between the impedance of the insulating layers (the passivating SiO_2 and the orienting polyimide) and that of the liquid crystal [32]. Consequently, the measured U_{th} value is certainly larger than the theoretical one [see

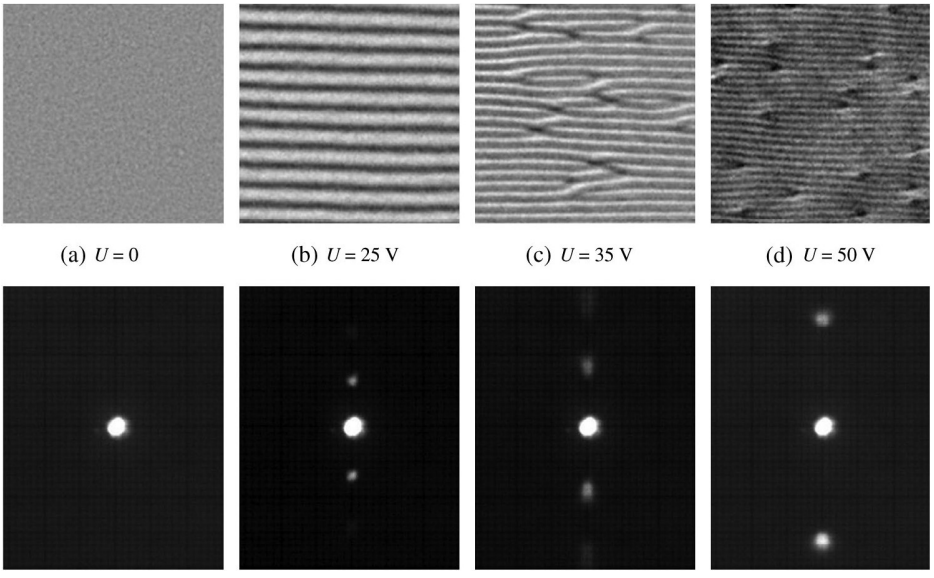

FIG. 2. Contrast-enhanced shadowgraph images (upper row; their size is $100 \times 100\ \mu$m) and the corresponding diffraction spots (lower row) of FDs at different voltages. (a) $U = 0$. (b) $U = 25$ V. (c) $U = 35$ V. (d) $U = 50$ V. The initial director alignment $\mathbf{n}_0$ is horizontal.

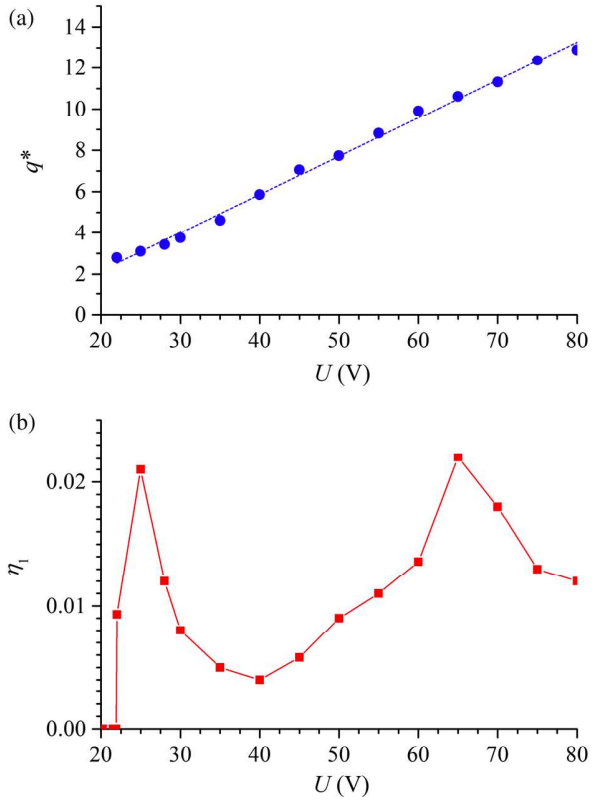

FIG. 3. Dependence of (a) the dimensionless wave number q^* of the pattern and (b) the diffraction efficiency η_1 of the first-order fringe on the applied dc voltage U.

Eq. (7)]. This fact should be taken into account during comparisons and application designs.

The feature shown in Eq. (5) is qualitatively similar to that reported previously for various calamitic LCs [18,33,34]; there, the α values deduced from published graphs fall into the range of 0.04–0.2 V^{-1}. Therefore, the linear dependence of q^* on voltage seems to be a general property of the flexoelectric domains in all LC systems; thus, it can serve as the basis for applying FDs in voltage-tunable LC gratings.

We note that, while the above-threshold (weakly nonlinear) behavior of EC patterns has been thoroughly investigated (both theoretically and experimentally), a similar detailed analysis of FDs is not yet available. The first theoretical attempt of describing the nonlinear behavior of FDs [19,29] ignored the anisotropy of the elastic properties (one-elastic-constant approximation) and, constraining themselves to high ($U \gg U_{\rm th}$) voltages, neglected the effect of the confining surfaces (no distortion across the sample). Under such assumptions, the calculation yielded [19,29]

$$U_{\rm th} = 0 \quad \text{and} \quad q^* = \alpha U, \quad \text{with} \quad \alpha \approx 0.4|e_1 - e_3|/K; \tag{6}$$

here, K is the single (averaged) elastic constant. Making a comparison with the experimental results in Eq. (5), we clearly see that the prediction of $q \propto U$ fails at low voltage [though Eq. (5) tends to Eq. (6) in the high-U limit], presumably because the threshold voltage is nonzero. It follows from the linear theory that the presence of an onset threshold is the consequence of the strong surface anchoring; hence, the anchoring effects must not be neglected when developing the nonlinear theory. Nevertheless, this has proved to be too big of a theoretical challenge thus far. To our knowledge, the only attempt [35] to overcome this problem did not provide data on $q(U)$ since only numerical results on the diffracted light intensities are reported.

Lacking rigorous nonlinear calculations and a resulting relation between the material parameters and the slope α of Eq. (5), we may only assume that the formula for α given in Eq. (6) provides a good approximation. With this assumption, using the measured value of α, the flexoelastic ratio $|e_1 - e_3|/K$ can be estimated as $|e_1 - e_3|/K = 0.46$ C/(N m), which is on the same order of magnitude as the corresponding parameter in calamitic materials [36]. The flexoelastic ratio can also be calculated independently from the critical wave number $q^*_{\rm th}$. Using the formulas obtained from the one-elastic-constant approximations [17],

$$U_{\rm th} = \frac{2\pi K}{|e_1 - e_3|(1+\mu)}, \qquad q^*_{\rm th} = \sqrt{\frac{1-\mu}{1+\mu}},$$
$$\mu = \frac{\varepsilon_0 \varepsilon_a K}{|e_1 - e_3|^2}, \tag{7}$$

and substituting the unknown dielectric anisotropy and elastic constant of 7*P*-CF_2O-ODBP with the values $\varepsilon_a = -4.3$ and $K = (K_1 + K_2)/2 = 10.62 \times 10^{-12}$ N measured for another member (9*P*-CF_2O-ODBP) of the same bent-core homologous series, we obtain $|e_1 - e_3|/K = 2.22$ C/(N m). Using this value, Eq. (7) yields $U_c = 10.4$ V for the theoretical threshold voltage. On the one hand, the large difference of the flexoelastic ratios provided by the two methods evidently points out the necessity of improving the theoretical description of the nonlinear regime as well as knowing the actual, not yet available material parameters of the studied compound. On the other hand, the deviation between the expected and measured thresholds proves the significance of the internal attenuation in the cell, which was mentioned above.

Increasing the applied dc voltage alters not only the positions of the diffraction spots (i.e., the value of $\mathbf{q}$) but also their intensity. Figure 3(b) exhibits how the diffraction efficiency $\eta_1 = I_1/I_0$—the ratio of the intensities corresponding to the first- (I_1) and the zeroth-order (I_0) diffraction spots—varies with the voltage up to about $4U_{\rm th}$. It is clearly seen that the voltage dependence is not monotonic. A previous calculation of the light intensities diffracted on an EC grating (where the director field is different from that of FDs) showed [37] that I_1 is there

described with a squared Bessel function $J_1^2(\beta U)$ (β is a combination of material and cell parameters), which is evidently nonmonotonic with the applied voltage. We are not aware of similar calculations for FDs. Though some numerical calculation of the diffracted intensities has been performed on a calamitic system [35], it covered only a much narrower voltage range (up to $1.5U_{th}$), which does not facilitate a comparison with the data in Fig. 3(b).

B. Polarization characteristics of the diffraction fringes

As the diffraction on LC gratings occurs due to the periodic refractive-index modulation caused by director distortions and the optical anisotropy, it is not surprising that the light intensity of a certain diffracted order depends strongly on the direction and polarization of the illuminating beam. For example, in the case of a standard EC [14–16], first-order spots are not visible at normal light incidence [37]. Moreover, only light with extraordinary polarization causes diffraction because, at ordinary illumination, there is no spatial refractive-index modulation.

Diffraction on FD gratings possesses some distinct features compared to the case of a standard EC which involve the intensity of fringes and the polarization of the diffracted light [38]. In Fig. 4, we summarize the typical

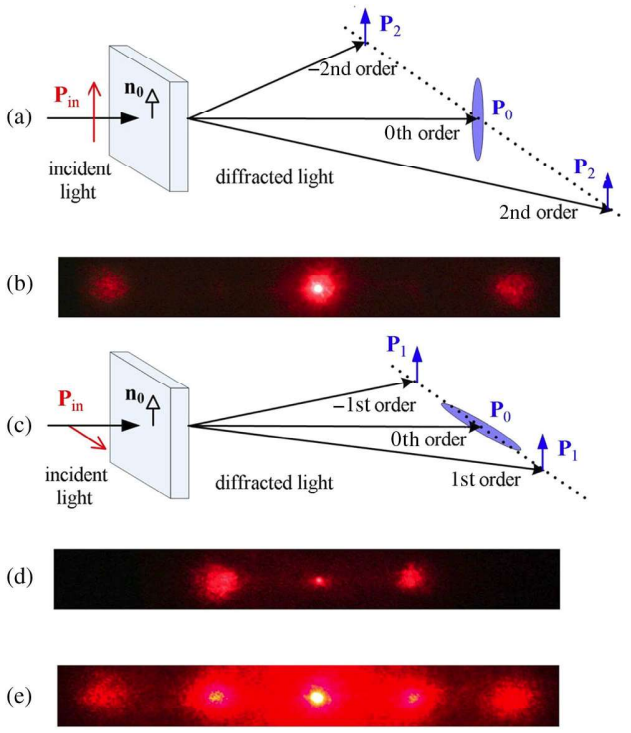

FIG. 4. Typical diffraction geometries and the corresponding diffraction images in a far screen. (a),(b) Incident light polarization $\mathbf{P}_{in}$ parallel with the initial director $\mathbf{n}_0$: only second-order diffraction spots are visible. (c),(d) $\mathbf{P}_{in}$ perpendicular to $\mathbf{n}_0$: only first-order diffraction spots are present. (e) $\mathbf{P}_{in}$ is oblique with respect to $\mathbf{n}_0$: both first- and second-order spots appear.

scenarios observed when the BCN sample is illuminated at normal incidence by a laser beam with a polarization direction $\mathbf{P}_{in}$ that is rotatable with respect to $\mathbf{n}_0$ and shows representative snapshots of the diffraction fringes in a far screen. The shape and the polarization of the diffraction spots are found to vary with the direction of $\mathbf{P}_{in}$:

Case A.—When $\mathbf{P}_{in} \| \mathbf{n}_0$ [Fig. 4(a), extraordinary illumination], the first-order spots vanish, whereas the second-order spots are present as shown in Fig. 4(b). Their polarization $\mathbf{P}_2$ is parallel with $\mathbf{P}_{in}$.

Case B.—If, however, $\mathbf{P}_{in} \perp \mathbf{n}_0$ [Fig. 4(c), ordinary illumination], the first-order spots are clearly seen. Their polarization $\mathbf{P}_1$ is perpendicular to $\mathbf{P}_{in}$, whereas the second-order spots disappear as depicted in Fig. 4(d).

Case C.—If $\mathbf{P}_{in}$ is oblique with respect to $\mathbf{n}_0$ [Fig. 4(e), superposition of ordinary and extraordinary illuminations], both the first- and second-order spots are visible.

In each case, the transmitted beam (zeroth-order spot) has a strongly elliptical polarization $\mathbf{P}_0$ with the long axis almost parallel with $\mathbf{P}_{in}$, which reflects the birefringence of the LC layer.

The observation in case A matches the behavior of standard EC [37]; case B is, however, specific to FDs. The complex three-dimensional (3D) director distortion in FDs involves not only out-of-plane (tilt), but also in-plane (azimuthal, twist) deformations. A recent theoretical analysis of the diffraction on general 3D director structures showed [39] that, in the presence of twist, the polarization of the diffracted light may be rotated by 90° with respect to that of the illuminating beam; thus, the observations above are in qualitative agreement with the theoretical predictions.

C. Dynamic behavior

While the static behavior presented above corresponds to the equilibrium (i.e., the final) state of the system, the dynamic behavior characterizes how this end state can be reached, e.g., after a voltage jump. Exploration requires the application of a biased square-wave driving signal (i.e., repetitive switching between two dc voltage levels, U_1 and U_2, with a period of τ_0, much larger than the growth or decay time of the pattern) and monitoring of the temporal evolution of the FDs in response to this voltage variation. Figure 5 shows the typical driving steplike waveform. The voltage jumps from U_1 to U_2 at the time instant $t = t_{up}$ and remains at that level for a duration of τ_1; then, at $t = t_{down} = t_{up} + \tau_1$, it jumps back to U_1 for a duration of τ_2. The sequence is repeated by the period of $\tau_0 = \tau_1 + \tau_2$. This waveform actually corresponds to a bipolar square wave of an amplitude of $(U_2 - U_1)/2$, biased with a dc voltage of $(U_1 + U_2)/2$.

Investigations of the switching characteristics by recording and processing image sequences shot by the camera imply that one has to distinguish between two cases. In case 1, the voltage is switched between values below and above the threshold, i.e., $U_2 > U_{th} > U_1$. This scenario corresponds to

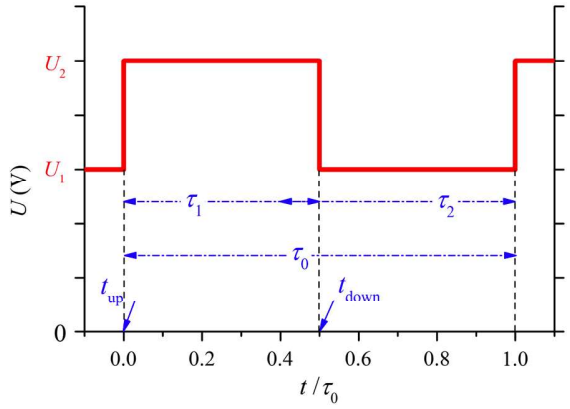

FIG. 5. One period of the steplike driving waveform.

repetitive decay and growth of the FD pattern. In case 2, both voltage levels are above the threshold, thus the switching occurs between two FD patterns of different wavelength. In the following we discuss the specialties of these two cases separately.

1. Case 1: $U_2 > U_{th} > U_1$

The threshold voltage of the FDs is found to be $U_{th} \lessapprox 22$ V. For studying the growth and decay of the FDs, we use the driving waveform shown in Fig. 5 with $\tau_1 = \tau_2 = \tau_0/2 = 50$ s. Figure 6 demonstrates the emergence and the decay of the FDs following the voltage jumps by a sequence of snapshots taken at regular intervals in the case of $U_1 = 15$ V and $U_2 = 25$ V. It can be seen from the snapshots that the wavelength does not seem to alter significantly during time elapsing; thus, the wavelength selection mostly occurs at the onset and the fastest growing mode is roughly the one finally seen in the equilibrium end state corresponding to U_2. Similarly, this wavelength also remains almost the same during decay. A detailed analysis shows, however, that the dimensionless averaged wave number $q^*_{av} = q_{av}d/\pi$ [see Eq. (3)] exhibits an increase of about 10%–20% at the beginning of the transient after the upward voltage jump, before reaching its final value as shown in Fig. 7. A decrease of the same order is detectable during the decay of the FDs. We note that this feature is slightly different from that reported for EC patterns [40], where no change of the wave number during decay is observed.

The characteristic times of the appearance and disappearance of the FD pattern are obtained by monitoring the temporal evolution of the pattern contrast. As the contrast C depends on the voltage U_2 [$C(U)$ increases with U in a certain voltage range], it is better to use the normalized contrast for a comparison of the time scales,

$$C^* = (C - C_{min})/(C_{max} - C_{min}), \tag{8}$$

shown in Fig. 8(a) for the growth and in Fig. 8(b) for the decay of FDs. Here, C_{max} and C_{min} are the maximal and minimal values of the contrast, respectively.

In the initial phase, immediately after the voltage increase, the pattern—and hence the contrast—grows exponentially ($C^* \propto \exp[(t - t_{up})/\tau_{growth}]$ for $C^* < 0.4$). Similarly, decreasing the voltage initiates an exponential decay of the pattern ($C^* \propto \exp[-(t - t_{down})/\tau_{decay}]$). The characteristic growth and decay times, τ_{growth} and τ_{decay}, can be obtained from the curves in Figs. 8(a) and 8(b), respectively, by exponential fitting. Alternatively, a switch-on time τ_{on} and a switch-off time τ_{off}—commonly used in display applications—can be defined as the time needed for the normalized contrast C^* to increase from 10% to 90% and to decrease from 90% to 10%, respectively.

All of these characteristic time values are collected in Table I. It is immediately seen that they all depend strongly on the value of U_2 (the larger the U_2, the shorter the τ_{growth}, τ_{decay}, τ_{on}, and τ_{off}). Variation of τ_{growth} with U_2 is not at all

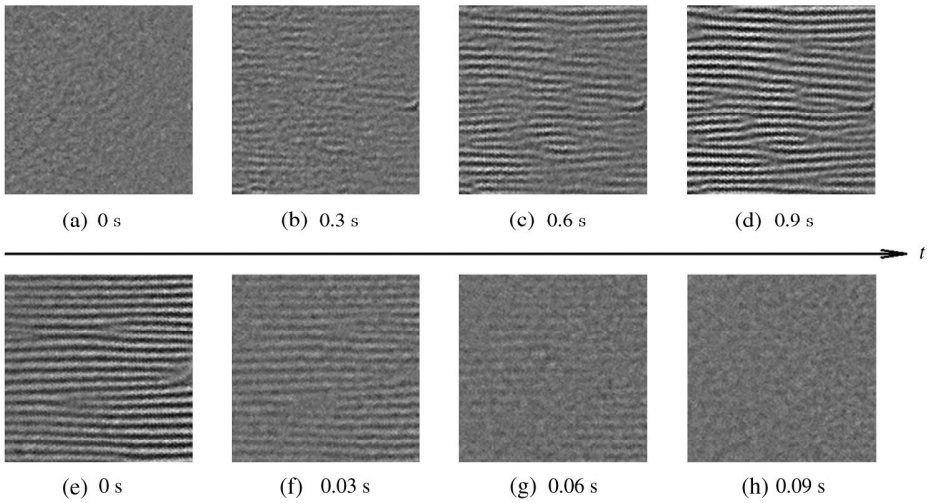

FIG. 6. Sequence of contrast-enhanced shadowgraph snapshots of the FD pattern during growth (voltage jumps from $U_1 = 15$ V to $U_2 = 25$ V, upper row) and decay (voltage jumps from $U_2 = 25$ V to $U_1 = 15$ V, lower row). The initial director $\mathbf{n}_0$ is horizontal. The time instants when the snapshots are taken are (a) $t = t_{up}$, (b) $t = t_{up} + 0.3$ s, (c) $t = t_{up} + 0.6$ s, (d) $t = t_{up} + 0.9$ s, (e) $t = t_{down}$, (f) $t = t_{down} + 0.03$ s, (g) $t = t_{down} + 0.06$ s, and (h) $t = t_{down} + 0.09$ s. The size of each snapshot is 100×100 μm. Contrast enhancement is performed by spanning the actual intensity range of the snapshots over the full intensity range.

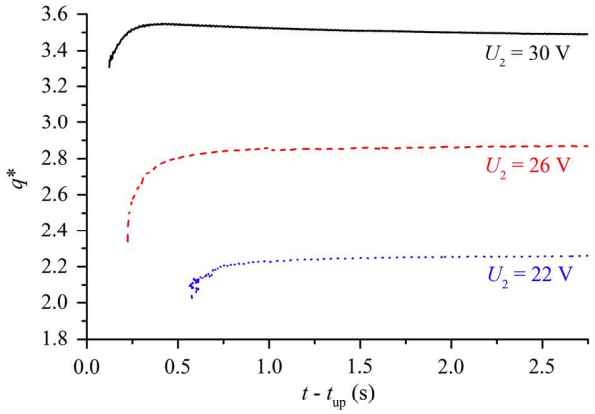

FIG. 7. Temporal evolution of the averaged dimensionless wave number q^*_{av} during the growth of FDs following a voltage jump from $U_1 = 18$ V (below threshold) to the indicated U_2 values. Time is counted from the instant $t = t_{up}$ of the voltage jump.

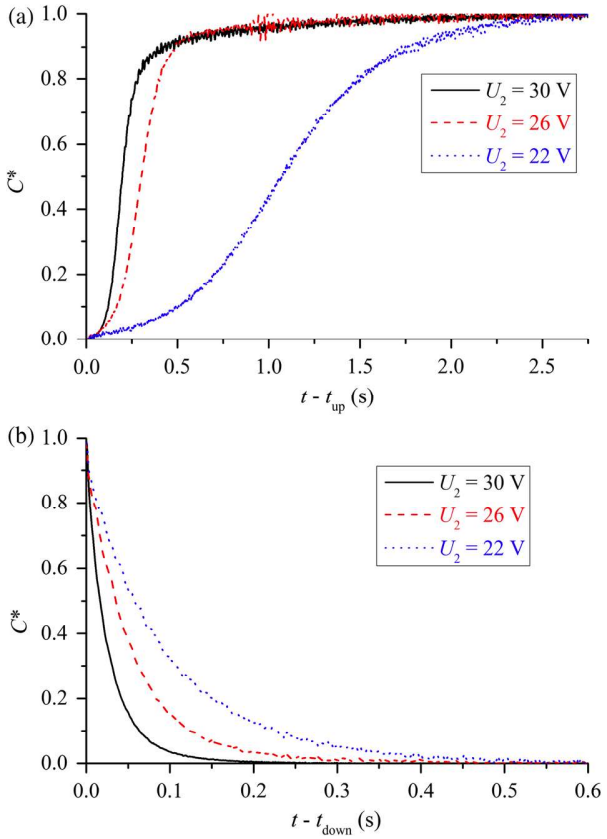

FIG. 8. Temporal evolution of the normalized contrast C^* (a) during the growth of FDs following a voltage jump from $U_1 = 18$ V (below threshold) to the indicated above-threshold U_2 values (time is counted from the instant $t = t_{up}$ of the voltage jump) and (b) during the decay of FDs following a voltage jump from the indicated U_2 values (above threshold) to the below-threshold value of $U_1 = 18$ V (time is counted from the instant $t = t_{down}$ of the voltage jump).

TABLE I. Characteristic times and q^{*2} of FDs vs the above-threshold voltage (U_2) at steplike driving with $U_1 = 18$ V and $\tau_0 = 100$ s. τ_d^* is the expected decay time when taking into account its dependence on q^{*2}.

U_2 (V)	τ_{growth} (s)	τ_{decay} (s)	τ_{on} (s)	τ_{off} (s)	q^{*2}	τ_d^* (s)
22	0.384	0.095	1.326	0.225	4.84	0.095
26	0.086	0.054	0.316	0.122	7.84	0.059
30	0.047	0.027	0.287	0.062	12.25	0.038

surprising since the growth of FDs is a typical field-driven effect. The decay, however, is a simple elastic relaxation; therefore, the voltage dependence is not evident. It may come from the fact that, at higher voltages, the pattern wavelength is shorter (i.e., q^* is larger; see Table I) and a pattern with a higher wave number decays faster. The latter has actually been proven theoretically as well as experimentally for the decay of the EC pattern [40], yielding a decay rate (τ_{decay}^{-1}) roughly proportional to q^{*2}. Assuming a similar dependence for the decay of the FDs would imply (see τ_d^* in Table I) a 1.6 times decrease of the decay time at $U_2 = 26$ V—and a 2.5 times lowering at $U_2 = 30$ V—compared to that at the near-threshold voltage of $U_2 = 22$ V; these values are quite close to the experimentally found ones. The deviation observed at high voltage may be due to the deformation getting out from the linear regime assumed in the calculations.

It is notable that the decay is much faster than the growth of the FDs. This result is evident from Table I; the time scales of the snapshots in Fig. 6 also prove that the decay or switch-off times are much shorter than the growth or switch-on times.

Figure 9 depicts the temporal evolution of the spectral entropy S defined in Eq. (2). Obviously, the appearance of

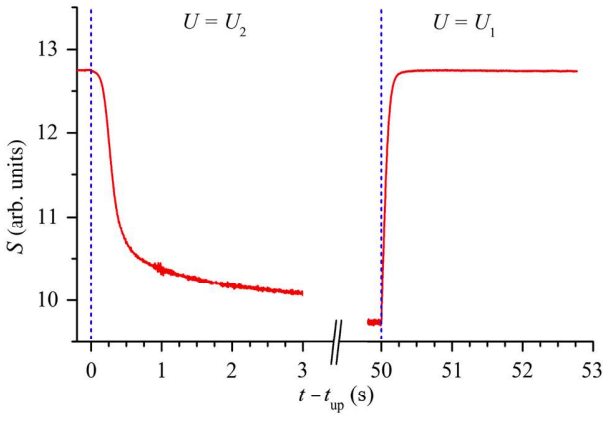

FIG. 9. Temporal evolution of the spectral entropy S when driven by a steplike waveform of Fig. 5 with $U_2 = 26$ V, $U_1 = 18$ V, and $\tau_1 = \tau_2 = \tau_0/2 = 50$ s. The left side corresponds to the voltage increase, the right side to the voltage decrease. Vertical dashed lines indicate the moments of voltage jumps.

FDs leads to a reduction of S, which increases back to its initial value in the homogeneous, pattern-free state during the decay of FDs. Thus, the temporal evolution of $S(t)$ is just the opposite of that of the pattern contrast $C(t)$.

2. Case 2: $U_2 > U_1 > U_{th}$

Under this condition, the BCN system switches alternately between two FD states. Namely, FD_2 with wavelength Λ_2 is present during the time interval τ_1 (while $U = U_2$), which transforms back to FD_1 with wavelength Λ_1 for the interval τ_2 (while $U = U_1$), and vice versa. While the wavelength varies, the orientation of the FD stripes remains the same during the transition process.

As both the FD_1 and the FD_2 states are patterned (none of them have a homogeneous director field), the mechanism of the transitions between these FD states differs considerably from the growth and decay processes described in Sec. III C 1, as we will prove below.

The characteristic features of the transition are demonstrated via evaluation of the image sequences recorded using a driving signal as in Fig. 5, characterized by $U_1 = 25$ V, $U_2 = 35$ V, and $\tau_1 = \tau_2 = \tau_0/2 = 50$ s. This low switching rate is selected so that it ensures reaching (or at least closely approaching) the final equilibrium states by the end of the intervals τ_1 and τ_2.

Figures 10, 11, and 12 depict the temporal evolution of the averaged dimensionless wave number q^*_{av}, the pattern contrast C, and the spectral entropy S, respectively, during the transition process following the voltage jumps.

We note first that, unsurprisingly, the transitions (the change of Λ from $\Lambda_1 \approx 4.6$ μm to $\Lambda_2 \approx 3.0$ μm and vice versa) are not instantaneous. Though the pattern contrast changes immediately after t_{up} or t_{down}, as opposed to the behavior found in Figs. 8 and 9 for the growth from or decay to the homogeneous state, the $C(t)$ curves in Fig. 11, as well as the $S(t)$ curves in Fig. 12, are nonmonotonic. Thus, in order to estimate the switching times of the $FD_1 \rightarrow FD_2$ transition, we should refer to the monotonic temporal variation of $q^*_{av}(t)$ in Fig. 10. It is obvious from the figure that q^*_{av} has not yet reached its final (equilibrium) value by the end of the presented interval of 7 s. It is also clear that the wave-number adjustment related to the upward voltage jump is much slower than that characterizing the downward voltage jump. Moreover, the switching times (on the order of seconds) are longer than those shown in Table I, which is characteristic for the pattern growth from or decay to the homogeneous state.

Let us now focus on the mechanism of the switching between two FD states, which is illustrated via some representative snapshots of the FDs in Figs. 13 and 14.

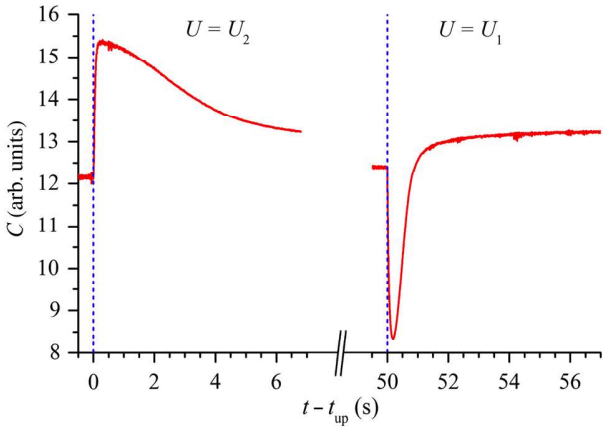

FIG. 11. Temporal evolution of the contrast C when driven by a steplike waveform of Fig. 5 with $U_1 = 25$ V, $U_2 = 35$ V, and $\tau_1 = \tau_2 = \tau_0/2 = 50$ s. The left side is at voltage increase, the right side is at voltage decrease. Vertical dashed lines indicate the moments of voltage jumps.

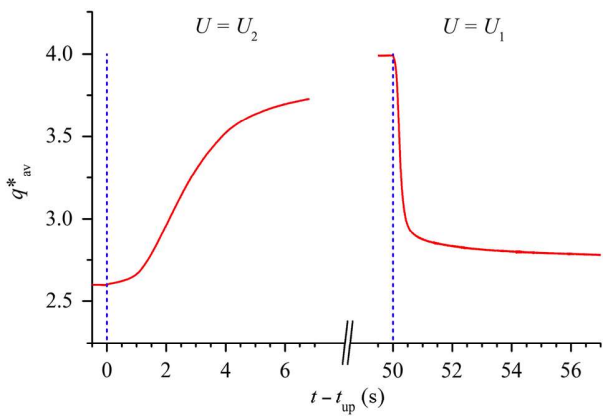

FIG. 10. Temporal evolution of the averaged dimensionless wave number q^*_{av} when driven by a steplike waveform of Fig. 5, with $U_1 = 25$ V, $U_2 = 35$ V, and $\tau_1 = \tau_2 = \tau_0/2 = 50$ s. The left side is at voltage increase, the right side is at voltage decrease. Vertical dashed lines indicate the moments of voltage jumps.

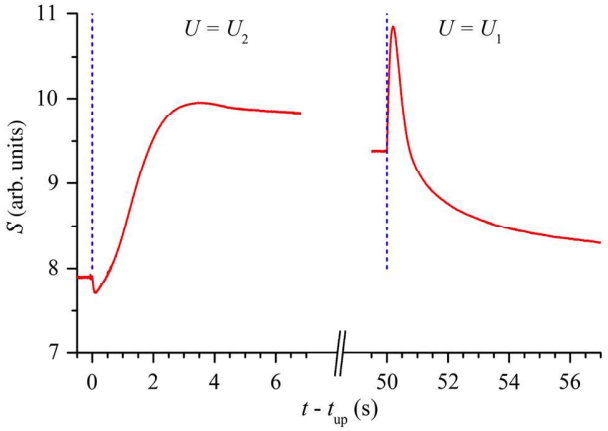

FIG. 12. Temporal evolution of the entropy S when driven by a steplike waveform of Fig. 5 with $U_1 = 25$ V, $U_2 = 35$ V, and $\tau_1 = \tau_2 = \tau_0/2 = 50$ s. The left side is at voltage increase, the right side is at voltage decrease. Vertical dashed lines indicate the moments of voltage jumps.

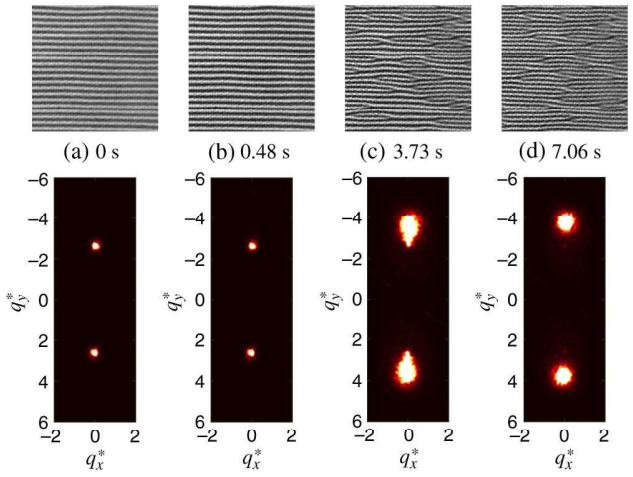

FIG. 13. Snapshots of the FD pattern (upper row; their size is 100×100 μm) and their FFT images (lower row) during the $FD_1 \rightarrow FD_2$ transition. (a) $t = t_{up}$, where voltage has just been increased from $U_1 = 25$ V to $U_2 = 35$ V. (b) $t = t_{up} + 0.48$ s, at the contrast maximum. (c) $t = t_{up} + 3.73$ s, at the maximum of the entropy. (d) $t = t_{up} + 7.06$ s, at the end of recording.

Based on these images and on the contrast curves of Fig. 11, the process of switching can be subdivided into two intervals.

The first is a short interval of about 0.5 s, immediately following the upward or downward voltage jumps, when a sudden change (increase or decrease, respectively) of the contrast and thus of the pattern amplitude is detected, without a substantial change of the wavelength. This amplitude change temporarily yields a higher (lower) pattern order, which is also manifested in the drop (increment) of the spectral entropy of Fig. 12.

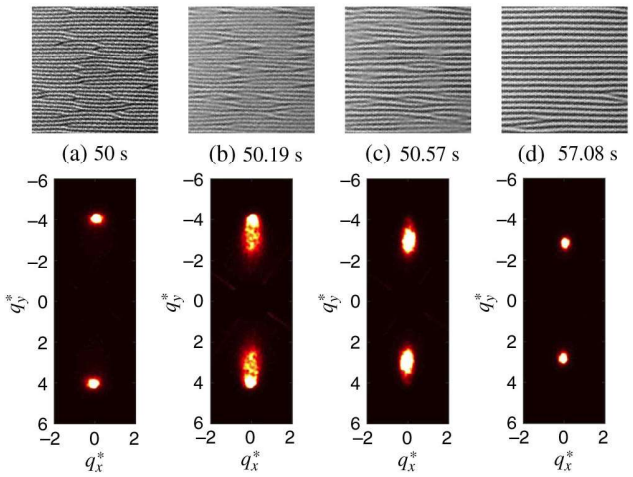

FIG. 14. Snapshots of the FD pattern (upper row; their size is 100×100 μm) and their FFT images (lower row) during the $FD_2 \rightarrow FD_1$ transition. (a) $t = t_{down} = t_{up} + 50$ s, where voltage has just been decreased from $U_2 = 35$ V to $U_1 = 25$ V. (b) $t = t_{down} + 0.19$ s, at the contrast minimum. (c) $t = t_{down} + 0.57$ s, at the maximum of the entropy. (d) $t = t_{down} + 7.08$ s, at the end of recording.

The second is the interval, when the actual adjustment of q occurs. Here, defects (dislocations) appear in pairs of opposite topological charge, which then move along the stripes in opposite directions until they reach the edge of the sample or annihilate with a defect of opposite topological charge, originating from another pair. This indicates that the pattern cannot tune its wavelength by continuously shrinking (or dilating) the width of the FD stripes; rather, the adjustment of Λ occurs via the generation and motion of defects. This mechanism is the same as the one reported for and investigated in detail in other stripe patterns (e.g., electroconvection) [41,42].

The presence of defects introduces disorder to the system, yielding an increase of the spectral entropy to a maximum value before relaxing to the equilibrium FD_2 state. As the defect creation and motion is driven by the wave-vector mismatch (the difference between the actual and the equilibrium q values), the growth phase ($\lesssim 3$ s) of S is much faster than the following relaxation ($\gg 10$ s). Note, however, that if $U_2 \gg U_{th}$ fulfills, FD_2 contains defects even in equilibrium, thus degrading the regularity of the

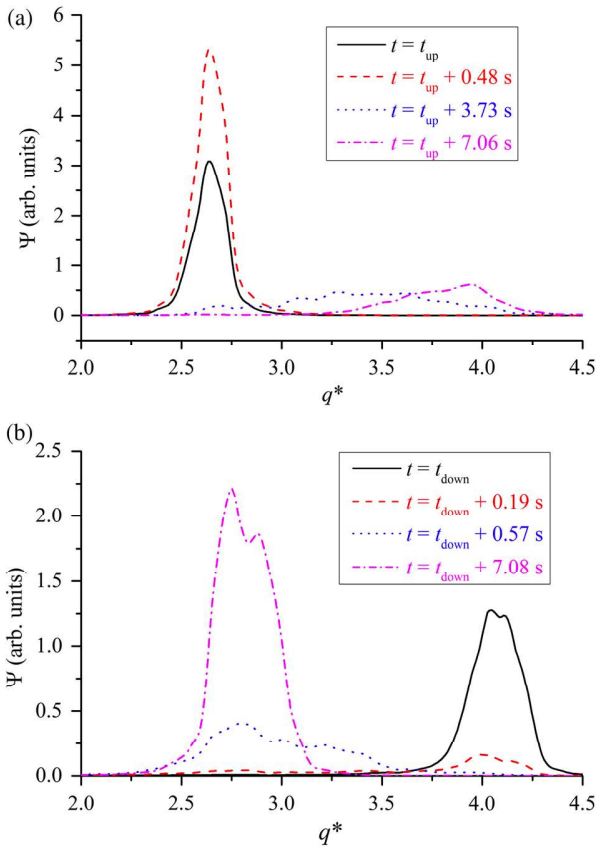

FIG. 15. Profile of the spectral distribution function Ψ along the q_x axis at different time moments following a voltage jump: (a) from $U_1 = 25$ V to $U_2 = 35$ V, and (b) from $U_2 = 35$ V to $U_1 = 25$ V.

pattern. Therefore, the spectral entropy in the FD_2 state will be larger than in the lower-voltage FD_1 state, as can be seen in Fig. 12. The disorder created by the defects is observable also in the FFT images belonging to the snapshots of Figs. 13 and 14. While the equilibrium FD states are characterized by sharp peaks in the Fourier space with the half-width of the FD_2 peak being larger than that of the FD_1 one, during the transient process, the Fourier transform is smeared and extends to a larger $\mathbf{q}$ range.

Figures 15(a) and 15(b) depict the profile of the spectral distribution function Ψ along the q_x axis in the Fourier space, at various time instants following the voltage jumping up and down, respectively. The figures also clearly show the delocalization of Ψ for a wide q range during the switching transient and prove that after upward voltage jumps more time is needed to reach the new equilibrium state than at voltage lowering.

IV. DISCUSSION AND CONCLUSIONS

The experimental results reported above point out some issues (e.g., the behavior of the contrast or the difference between switching on and off) which are worth further discussing.

The contrast of the shadowgraph image of the FD pattern depends on the magnitude of the periodic director distortions. The latter, as well as the wave number of the FDs, should be the outcome of a rigorous nonlinear theoretical analysis, which is not currently available. Even without that, some qualitative conclusions can be drawn. FDs correspond to an equilibrium deformation, characterized by the balance of the destabilizing flexoelectric and the stabilizing elastic and dielectric torques. Their existence proves that, in a certain voltage range, the reduction of the free energy of the deformed state due to the flexoelectric contribution overcomes the increments due to the elastic and dielectric terms. Increasing the voltage increments the flexoelectric torque, which thus has to be compensated for by higher stabilizing torques. The latter may be reached either by an increase of the pattern amplitude (the director deviation angle), a reduction of the wavelength (an increase of the director gradients), or a combination thereof.

The measurements clearly show the substantial dependence of the wavelength on the applied voltage [see Figs. 3(a), 10, 13, and 14]. Because of that, the new torque balance at a higher voltage can be reached by a moderate increase of the pattern amplitude, resulting in some increase of the pattern contrast. By contrast, in the initial phase of the switching transient when the wavelength is still unaltered, the torque increase due to the upward voltage jump should be fully compensated for by the change of the pattern amplitude only. This is the reason for the sudden jump in the contrast of the pattern in Fig. 11. As the wavelength starts to adjust itself to the shorter final value, the pattern amplitude relaxes to a much lower level. Similarly, after a downward voltage jump, the balance with a reduced flexoelectric torque can be reached by a much lower pattern amplitude (where the pattern almost disappears), as is indicated in Fig. 11 by the sudden drop of the contrast. Again, as the wavelength adjustment starts operating, the pattern amplitude—and thus the contrast—relaxes, now to a higher value due to wavelength lengthening.

A remarkable feature of FD dynamics is that the response to voltage decrement is much faster than that upon voltage increment. At first glance, this finding seems to be counterintuitive, as it is a common experience with LCDs that the switch-on times can be substantially reduced by increasing the voltage. A closer look at the equations shows, however, that this acceleration of the switching occurs only at high enough voltage, but it does not work at a voltage close to the threshold. This can be easily demonstrated in the simple case of the twist Fréedericksz transition (FT), where analytical expressions for the switching-on (τ_{on}) and the switching-off (τ_{off}) time constants are available [2,43,44]:

$$\tau_{off} = \frac{\gamma_1 \pi^2}{K_2 d^2}, \qquad \tau_{on} = \tau_{off} \frac{1}{(\frac{U}{U_F})^2 - 1}. \tag{9}$$

Here, γ_1 is the rotational viscosity, K_2 is the twist elastic constant and U_F is the twist Fréedericksz threshold voltage. It is seen from Eq. (9) that, indeed, $\tau_{on} \ll \tau_{off}$ for $U \gg U_F$; however, τ_{on} diverges as $U \to U_F$. As a consequence, for $U < 1.4U_F$, one finds $\tau_{on} > \tau_{off}$.

For flexodomains, switching on is a field-driven process, while switching off is an elastic relaxation, just as in the FT. Therefore, similar tendencies are expected for FDs as for the FT: acceleration at high voltage, but slowing down near the threshold. The U/U_{th} ratio used during the measurements in Fig. 6 is about 1.14; i.e., being much below the value calculated above, the $\tau_{on} > \tau_{off}$ relation should not be surprising. Nevertheless, the dynamics of the FDs is a much more complex phenomenon than that of the twist Fréedericksz transition (e.g., the linear flexoelectric interaction is also involved) and, unfortunately, no analytical solutions have yet been derived for its time scale(s). Therefore, it is still unclear how this complexity affects the temporal behavior.

The linear voltage dependence of the wave number [Eq. (5)] offers a possibility for the creation of optical gratings, tunable or switchable by a dc voltage. We have shown that switching between two FD states of different wavelength has a different mechanism compared to the switching between a FD and the homogeneous initial state. The transition necessarily involves the creation and motion of dislocations, which considerably slows the response. Therefore, if repetitive switching between FD states is required, the switching frequency has to be fairly low. During the measurements, an ultralow frequency of $f = 10$ mHz ($\tau_0 = 100$ s) is used, which ensures switching between (quasi)equilibrium final FD states.

If the repetition rate is too large (i.e., if τ_0 is not long enough), the transition process cannot complete adequately; the system will not reach the final FD_1 or FD_2 equilibrium states; instead, it will switch between intermediate, nonequilibrium states. These intermediate states are characterized by a nonsaturated average wave vector [Eq. (4)] and a reduced order of the resulting pattern (a large number of defects), which depends on the magnitude of τ_0.

In the end, it is worth mentioning the potential of FDs in applications by their capability of wavelength tuning. FDs as tunable optical gratings may be used for laser scanning and beam steering (e.g., in microscopy or in LIDAR applications). Compared to current solutions like piezoelectric scanning mirrors or acousto-optical deflectors, a FD-based device is simple: it has no moving mechanical parts and no requirements of special driving. Its operating voltage is lower and has convenient linear characteristics, and the size of a deflector unit can be made very small. Its drawback, relatively low diffraction efficiency, can be improved by tuning the material parameters: towards higher birefringence or via doping by dichroic dyes. Based on our current experimental results shown in Fig. 3(a), a beam-steering device can be constructed whose light deflection (first-order diffracted light with an illumination wavelength of 0.65 μm) of 0°–10° can be obtained with linear dependence in the voltage range of 22–40 V. The scanning performance can be enhanced by using polarizers to eliminate the influences of other (zeroth and second) diffraction orders.

V. SUMMARY

In this paper, we investigate the static and dynamic characteristics of flexoelectric-effect-driven pattern formation in a BCN system. We show that the wave number of the FDs are adjustable linearly in a wide range by a relatively low dc voltage, offering their application as tunable optical gratings. The decay time of the gratings is found to be significantly smaller than the growth time, which we explain qualitatively in analogy with the dynamics of the Fréedericksz transition. We point out the importance of the defect generation and annihilation during the process of wave-number changing, where we find larger switching times in the case where the initial state is characterized by a lower wave number. We find that the phenomena under our scope are worth considering as a potential alternative of current methods for laser scanning or beam-steering applications, especially where the small size, the simplicity, and the low cost of the tunable optical grating device is important.

ACKNOWLEDGMENTS

We thank W. Pesch and A. Krekhov for the illuminating discussions. This work was supported by the National Natural Science Foundation of China (Grants No. 11374067 and No. 11374087), the Guangdong Provincial Science and Technology Plan (Grants No. 2014A050503064 and No. 2016A050502055), the Hungarian Research Fund (Grant No. OTKA NN110672), and the 2012 Inter-Governmental S&T Cooperation Proposal between Hungary and China (6-8 Complex study of nonlinear structures in novel types of liquid crystals, TÉT_12_CN-1-2012-0039).

[1] P. G. de Gennes and J. Prost, *The Physics of Liquid Crystals* (Oxford Science Publications, Oxford, 2001).

[2] L. M. Blinov and V. G. Chigrinov, *Electrooptic Effects in Liquid Crystal Materials* (Springer, New York, 1996).

[3] I. C. Khoo, Nonlinear optics, active plasmonics and metamaterials with liquid crystals, Prog. Quantum Electron. **38**, 77 (2014).

[4] W. Lee and S. T. Wu, Focus issue introduction: Liquid crystal materials for photonic applications, Opt. Mater. Express **1**, 1585 (2011).

[5] J. Kim, J. H. Suh, B. Y. Lee, S. U. Kim, and S. D. Lee, Optically switchable grating based on dye-doped ferroelectric liquid crystal with high efficiency, Opt. Express **23**, 12619 (2015).

[6] Z. Zheng, Y. Li, H. K. Bisoyi, L. Wang, T. J. Bunning, and Q. Li, Three-dimensional control of the helical axis of a chiral nematic liquid crystal by light, Nature (London) **531**, 352 (2016).

[7] J. Chen, P. J. Bos, H. Vithana, and D. L. Johnson, An electro-optically controlled liquid crystal diffraction grating, Appl. Phys. Lett. **67**, 2588 (1995).

[8] S. M. Morris, D. J. Gardiner, F. Castles, P. J. W. Hands, T. D. Wilkinson, and H. J. Coles, Fast-switching phase gratings using in-plane addressed short-pitch polymer stabilized chiral nematic liquid crystals, Appl. Phys. Lett. **99**, 253502 (2011).

[9] J. L. Zhu, J. G. Lu, J. Qiang, E. W. Zhong, Z. C. Ye, Z. H. He, X. J. Guo, C. Y. Dong, Y. K. Su, and H. P. D. Shieh, 1D/2D switchable grating based on field-induced polymer stabilized blue phase liquid crystal, J. Appl. Phys. **111**, 033101 (2012).

[10] P. Pagliusi and G. Cipparrone, Photorefractive effect due to a photoinduced surface-charge modulation in undoped liquid crystals, Phys. Rev. E **69**, 061708 (2004).

[11] H. C. Jau, T. H. Lin, Y. Y. Chen, C. W. Chen, J. H. Liu, and Andy Y. G. Fuh, Direction switching and beam steering of cholesteric liquid crystal gratings, Appl. Phys. Lett. **100**, 131909 (2012).

[12] Y. Xiang, Y. K. Liu, T. Li, S. L. Yang, and Z. J. Jiang, Laser induced gratings enhanced by surface-charge mediated electric field in doped nematic liquid crystals, J. Appl. Phys. **104**, 063107 (2008).

[13] Ming-Ya Xu, Yi-Kun Liu, Ying Xiang, Tian Xia, Everett Wang, and Zheng-Dong Cheng, A fast light-induced grating in bent-core nematic liquid crystals with in-plane switching, Appl. Phys. Lett. **103**, 083507 (2013).

[14] L. Kramer and W. Pesch, in *Pattern Formation in Liquid Crystals*, edited by Á. Buka and L. Kramer (Springer-Verlag, New York, 1996), p. 221.
[15] Á. Buka, N. Éber, W. Pesch, and L. Kramer, in *Self Assembly, Pattern Formation and Growth Phenomena in Nano-Systems*, edited by A. A. Golovin and A. A. Nepomnyashchy (Springer, Dordrecht, 2006), p. 55.
[16] N. Éber, P. Salamon, and Á. Buka, Electrically induced patterns in nematics and how to avoid them, Liq. Cryst. Rev. **4**, 101 (2016).
[17] Yu. P. Bobylev and S. A. Pikin, Threshold piezoelectric instability in a liquid crystal, Zh. Eksp. Teor. Phys. **72**, 369 (1977) [Sov. Phys. JETP **45**, 195 (1977)].
[18] M. I. Barnik, L. M. Blinov, A. N. Trufanov, and B. A. Umanski, Flexo-electric domains in liquid crystals, J. Phys. (Paris) **39**, 417 (1978).
[19] S. A. Pikin, *Structural Transformations in Liquid Crystals* (Gordon and Breach Science Publishers, New York, 1991).
[20] *Flexoelectricity in Liquid Crystals: Theory, Experiments and Applications*, edited by Á. Buka and N. Éber (Imperial College Press, London, 2012).
[21] Á. Buka, T. Tóth-Katona, N. Éber, A. Krekhov, and W. Pesch, in *Flexoelectricity in Liquid Crystals: Theory, Experiments and Applications*, edited by Á. Buka and N. Éber (Imperial College Press, London, 2012), Chap. 4, pp. 101–135.
[22] H. Takezoe and Y. Takanishi, Bent-core liquid crystals: Their mysterious and attractive world, Jpn. J. Appl. Phys. **45**, 597 (2006).
[23] A. Jákli, Liquid crystals of the twenty-first century—Nematic phase of bent-core molecules, Liq. Cryst. Rev. **1**, 65 (2013).
[24] A. Jákli, J. Harden, and N. Éber, in *Flexoelectricity in Liquid Crystals: Theory, Experiments and Applications*, edited by Á. Buka and N. Éber (Imperial College Press, London, 2012), Chap. 3, pp. 61–99.
[25] J. Hardeen, B. Mbanga, N. Éber, K. Fodor-Csorba, S. Sprunt, J. T. Gleeson, and A. Jákli, Giant Flexoelectricity of Bent-Core Nematic Liquid Crystals, Phys. Rev. Lett. **97**, 157802 (2006).
[26] J. Harden, R. Teeling, J. T. Gleeson, S. Sprunt, and A. Jákli, Converse flexoelectric effect in a bent-core nematic liquid crystal, Phys. Rev. E **78**, 031702 (2008).
[27] K. V. Le, F. Araoka, K. Fodor-Csorba, K. Ishikawa, and H. Takezoe, Flexoelectric effect in a bent-core mesogen, Liq. Cryst. **36**, 1119 (2009).
[28] B. Kundu, A. Roy, R. Pratibha, and N. V. Madhusudana, Flexoelectric studies on mixtures of compounds made of rodlike and bent-core molecules, Appl. Phys. Lett. **95**, 081902 (2009).
[29] E.-M. Terentev and S. A. Pikin, Nonlinear effects in a real flexoelectric structure, Zh. Eksp. Teor. Fiz. **83**, 1038 (1982) [Sov. Phys. JETP **56**, 587 (1982)].
[30] S. Rasenat, G. Hartung, B. L. Winkler, and I. Rehberg, The shadowgraph method in convection experiments, Exp. Fluids **7**, 412 (1989).
[31] K. E. Daniels, O. Brausch, W. Pesch, and E. Bodenschatz, Competition and bistability of ordered undulations and undulation chaos in inclined layer convection, J. Fluid Mech. **597**, 261 (2008).
[32] N. Éber, L. O. Palomares, P. Salamon, A. Krekhov, and Á. Buka, Temporal evolution and alternation of mechanisms of electric field induced patterns at ultra-low-frequency driving, Phys. Rev. E **86**, 021702 (2012).
[33] P. Kumar and K. S. Krishnamurthy, Gradient flexoelectric switching response in a nematic phenyl benzoate, Liq. Cryst. **34**, 257 (2007).
[34] P. Salamon, N. Éber, Á. Buka, T. Ostapenko, S. Dölle, and R. Stannarius, Magnetic control of flexoelectric domains in a nematic fluid, Soft Matter **10**, 4487 (2014).
[35] A. Cama, P. Galatola, C. Oldano, and M. Rajteri, Non-linear theory of flexoelectrically induced periodic distortions in nematic liquid crystals, Mol. Cryst. Liq. Cryst. **261**, 177 (1995).
[36] N. Éber, in *Flexoelectricity in Liquid Crystals: Theory, Experiments and Applications*, edited by Á. Buka and N. Éber (Imperial College Press, London, 2012), Appendix A, pp. 249–265.
[37] T. John, U. Behn, and R. Stannarius, Laser diffraction by periodic dynamic patterns in anisotropic fluids, Eur. Phys. J. B **35**, 267 (2003).
[38] Ming-Ya Xu, Meng-jie Zhou, Ying Xiang, Péter Salamon, Nándor Éber, and Ágnes Buka, Domain structures as optical gratings controlled by electric field in a bent-core nematic, Opt. Express **23**, 15224 (2015).
[39] W. Pesch and A. Krekhov, Optical analysis of spatially periodic patterns in nematic liquid crystals: Diffraction and shadowgraphy, Phys. Rev. E **87**, 052504 (2013).
[40] N. Éber, S. A. Rozanski, S. Németh, Á. Buka, W. Pesch, and L. Kramer, Decay of spatially periodic patterns in a nematic liquid crystal, Phys. Rev. E **70**, 061706 (2004).
[41] E. Bodenschatz, W. Pesch, and L. Kramer, Structure and dynamics of dislocations in anisotropic pattern forming systems, Physica (Amsterdam) **32D**, 135 (1988).
[42] S. Nasuno, S. Takeuchi, and Y. Sawada, Motion and interaction of dislocations in electrohydrodynamic convection of nematic liquid crystals, Phys. Rev. A **40**, 3457 (1989).
[43] Deng-Ke Yang and Shin-Tson Wu, *Fundamentals of Liquid Crystal Devices* (John Wiley & Sons, Chichester, England, 2006), p. 144.
[44] M. Khazimullin, T. Müller, S. Messlinger, I. Rehberg, W. Schöpf, A. Krekhov, R. Pettau, K. Kreger, and H.-W. Schmidt, Gel formation in a mixture of a block copolymer and a nematic liquid crystal, Phys. Rev. E **84**, 021710 (2011).